Supplementary material: Detection and characterization of discontinuous motion on Thompson Glacier, Canadian High Arctic, using synthetic aperture radar speckle tracking and ice-flow modeling

Giovanni CORTI,[1] Bernhard RABUS,[2] Gwenn E. FLOWERS[1]

[1]*Department of Earth Sciences, Simon Fraser University, Burnaby, BC, Canada*
[2]*Department of Engineering Sciences, Simon Fraser University, Burnaby, BC, Canada*
Correspondence: Giovanni Corti <gcorti@sfu.ca>

SCENE DETAILS

Table S1 gives details for all RADARSAT-2 scenes used in this study with Fig. S1 showing the corresponding footprints.

EMPIRICAL BIAS CORRECTION

Several additional processing steps are carried out post-speckle tracking to ensure accurate results. As intensity transformations increase the shift bias in GAMMA's `offset_pwr_tracking`, a bias correction is desirable. We perform an empirical bias correction by creating a synthetic 20000×3000 pixel speckle pattern, transforming the intensities and applying a linearly increasing shift, along the shorter axis of the speckle pattern, using a 2-D fast Fourier transform. Speckle tracking is then run on the original synthetic speckle and stretched images, using the same upsampling configuration as the real data speckle tracking, a 1 pixel step in the stretch direction and a 100 pixel step in the stretch-perpendicular direction. The results are averaged in the stretch perpendicular direction and 1-D interpolation is used to achieve a function that relates the measured shift to the shift bias. An empirical bias correction is then carried out using this function.

Next, a topographic correction is applied that accounts for the shifts between different SAR images due to local topography and differing acquisition positions (i.e., the spatial baseline of the image pair). For this

Mode	Incidence Angle (°)	Date 1	Date 2	Avg. NCC
SLA7	35.3	2018-01-31	2018-02-24	0.295
SLA7	35.3	2018-02-24	2018-03-20	0.300
SLA7	35.3	2018-03-20	2018-04-13	0.301
SLA7	35.3	2018-04-13	2018-05-07	0.229
SLA7	35.3	2022-01-05	2022-01-29	0.329
SLA7	35.3	2022-01-29	2022-02-22	0.399
SLA7	35.3	2022-02-22	2022-03-18	0.254
SLA21	45.3	2018-02-15	2018-03-11	0.277
SLA21	45.3	2018-03-11	2018-04-04	0.270
SLA21	45.3	2018-04-04	2018-04-28	0.210
SLA21	45.3	2018-04-28	2018-05-22	0.163
SLA21	45.3	2022-01-01	2022-01-25	0.172
SLA21	45.3	2022-01-25	2022-02-18	0.320
SLA21	45.3	2022-02-18	2022-03-14	0.165
SLA70	20.4	2015-03-17	2015-04-10	0.231
SLA70	20.4	2015-04-10	2015-05-04	0.238
SLA70	20.4	2018-02-05	2018-03-01	0.321
SLA70	20.4	2018-03-01	2018-03-25	0.279
SLA70	20.4	2018-03-25	2018-04-18	0.276
SLA71	21.5	2012-12-28	2013-01-21	0.217
SLA71	21.5	2013-01-21	2013-02-14	0.323
SLA71	21.5	2014-01-16	2014-02-09	0.264
SLA71	21.5	2014-02-09	2014-03-05	0.288
SLA71	21.5	2014-03-05	2014-03-29	0.218
SLA71	21.5	2018-02-07	2018-03-03	0.364
SLA71	21.5	2018-02-12	2018-03-08	0.308
SLA71	21.5	2018-03-03	2018-03-27	0.324
SLA71	21.5	2018-03-08	2018-04-01	0.294
SLA71	21.5	2018-03-27	2018-04-20	0.321
SLA71	21.5	2018-04-01	2018-04-25	0.275

Table S1. List of speckle tracking scene pairs. "Mode" refers to a RADARSAT2-specific designation of the scene pair imaging geometry. "Avg. NCC" denotes the mean normalized cross correlation from the speckle tracking results, a measure of the temporal (weather-related) decorrelation between scenes. Dates are in the YYYY-MM-DD format.
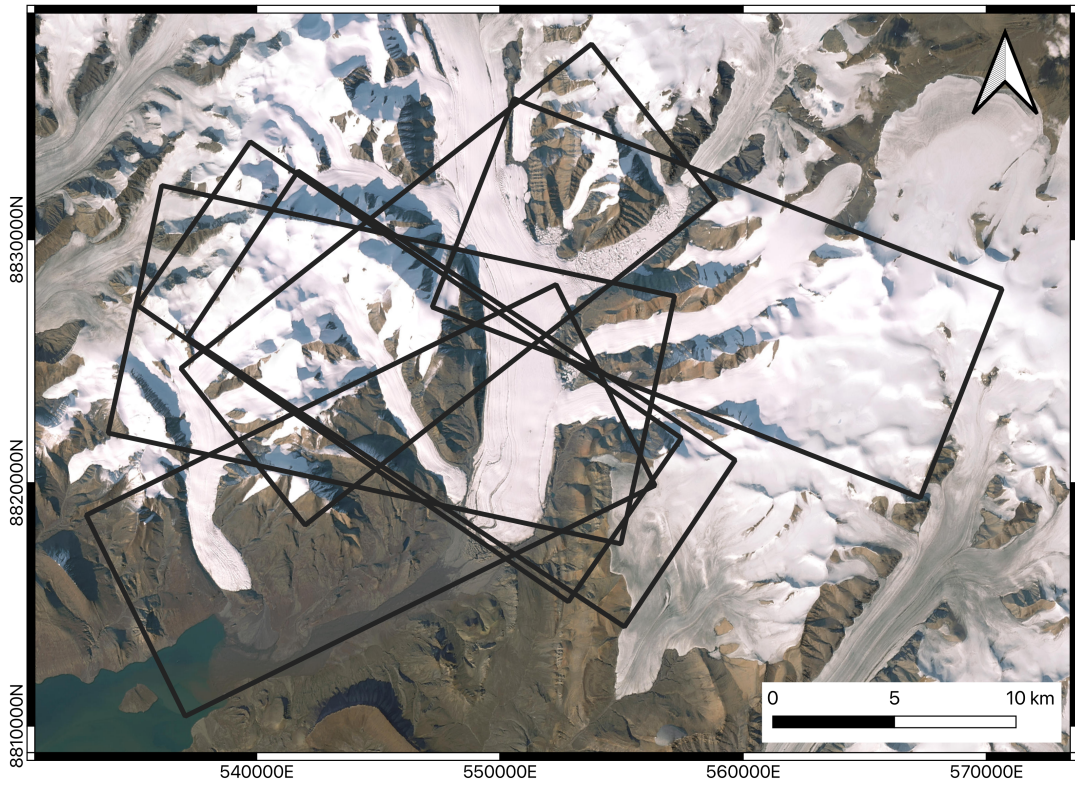
Fig. S1. Footprints for all SAR scenes listed in Table S1. Scenes with almost identical footprints have been grouped together. Optical imagery courtesy of Esri World Imagery (Esri, 2022).

correction a topographic shift maps is generated using GAMMA's `rdc_trans` program, which uses a DEM in the SAR geometry (i.e., a DEM that has been transformed to align with the SAR image) along with the satellite orbit information. As with the rest of this study, ArcticDEM (Porter and others, 2018) is used as the DEM. Then, a second coregistration, where all non-static terrain in the SAR image is masked out (according to GLIMS outlines (GLIMS Consortium, 2005) of the glaciers and manually delineated masks of large, ice covered lakes) is applied to ensure accurate coregistation. This second coregistration is designed to eliminate misregistration that may occur if GAMMA's standard coresigstration algorithm mistakes slow moving ice for static terrain.

BROKEN FRINGES FOR OTHER CHANNELS

Interferograms of both the West (Fig. S2) and Upper (Fig. S3) channels show broken fringes. As is the case with the Astro Channel, these fringes are not sensitive to variations in the perpendicular baseline, indicating that discontinuous motion is occurring across the channels.

VELOCITY PROFILES FOR OTHER CHANNELS

We plot velocity profiles by sampling 3-D velocity rasters across transects that run perpendicular to both the West (Fig. S4) and Upper (Fig. S5) Channels. In both cases, the cross-channel velocity gradients are consistent with the overall velocity gradients of the profiles, suggesting that no measurable cross-channel velocity discontinuity is present.

ICE-FLOW MODELING DETAILS

The thermal conductivity of pure ice is given by

$$k(T) = 9.828 \exp(-5.7 \times 10^{-3} T), \tag{S1}$$

where T is ice temperature in Kelvin (Cuffey and Paterson, 2010). For the ice-flow model employed in this study, the nonlinear dependence of (S1) on temperature would require a computationally expensive process such as Picard iteration to solve. However, (S1) is nearly linear over the range of plausible temperatures used in this model. Thus, we linearize (S1) for the $-25°$C to $0°$C range through ordinary least squares regression to obtain $k(T) = 2.0619 - 0.0127\,T$ where T is the temperature in $°$C.
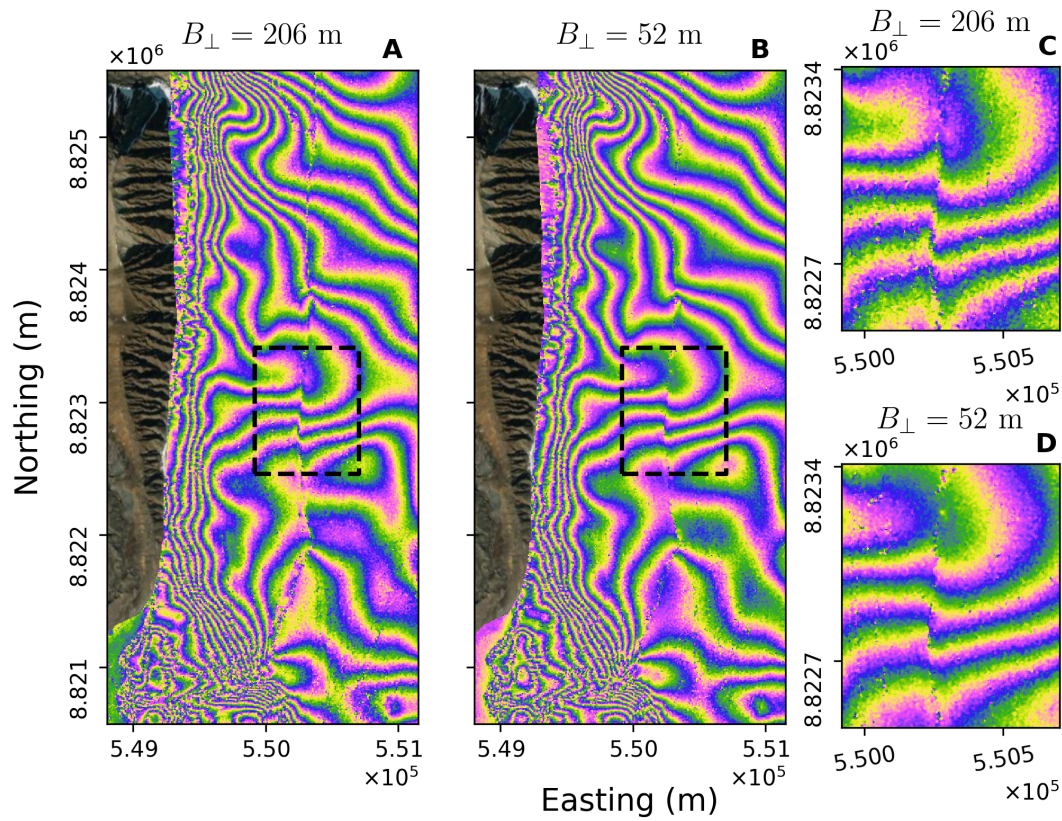
Fig. S2. A comparison of consecutive interferograms with differing baselines for the discontinuity across the West Channel of Thompson Glacier. The interferogram in (a) is created using data from 15 February 2018 and 11 March 2018. The interferogram in (b) is created using data from 11 March 2018 and 4 April 2018. Panels (c) and (d) focus on the broken fringes, showing enlarged versions of the fringe patterns contained in the black boxes in (a) and (b), respectively. Note that despite the significant difference in $B_\perp$, the magnitude of the fringe discontinuities is approximately equal in both interferograms, indicating discontinuous motion as opposed to discontinuous topography. Optical imagery courtesy of Esri World Imagery (Esri, 2022).
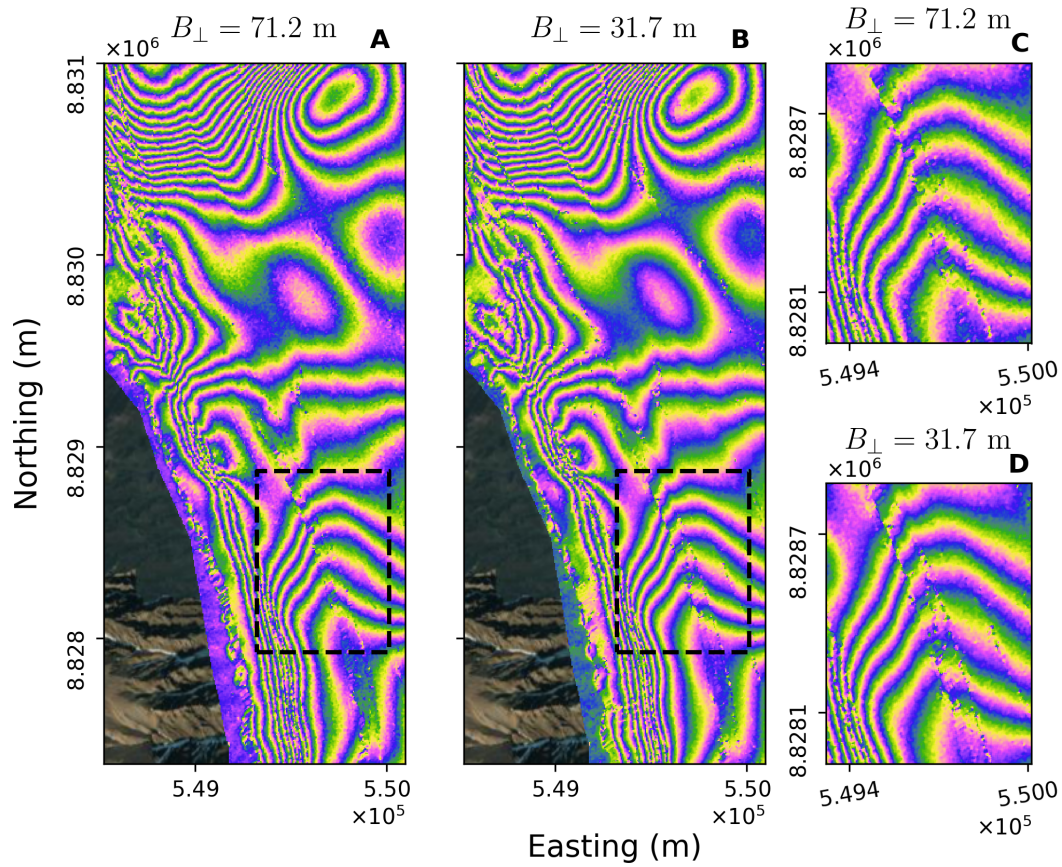
Fig. S3. A comparison of consecutive interferograms with differing baselines for the discontinuity across the Upper Channel of Thompson Glacier. The interferogram in (a) is created from SAR data collected on 7 February 2018 and 3 March 2018 (b) is created from SAR data collected on 3 March 2018 and 27 March 2018. Panels (c) and (d) focus on the broken fringes, showing enlarged versions of the fringe patterns contained in the black boxes in (a) and (b) respectively. Note that despite the significant difference in $B_\perp$, the magnitude of the fringe discontinuities is approximately equal in both interferograms, indicating discontinuous motion as opposed to discontinuous topography. Optical imagery courtesy of Esri World Imagery (Esri, 2022).
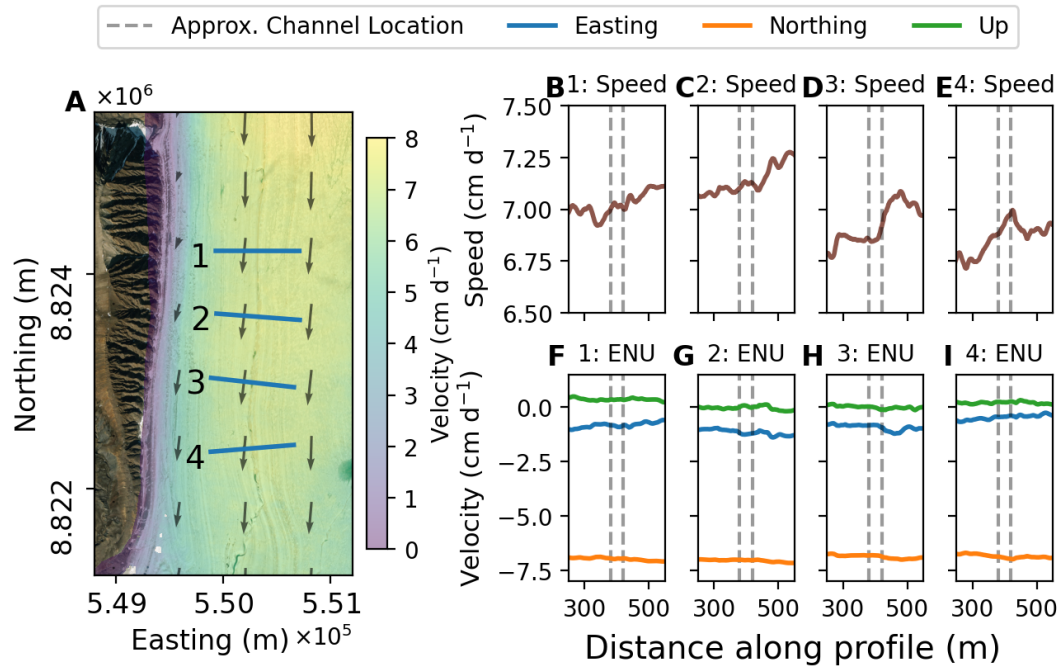
Fig. S4. 1-D profiles across the West Channel from 3-D inversion results from the 29 January 2022 and 22 February 2022 (ascending) and 25 January 2022 and 18 February 2022 (descending) scene pairs. The location and number of each profile is shown in (a) and the speed along the profile is shown in (b–e). The profile velocity results, separated into ENU components are shown in (f–i). The dashed black lines in (b–i) indicate the approximate location of the channel as obtained from manual delineation of the channel in optical satellite imagery. Optical imagery courtesy of Esri World Imagery (Esri, 2022).
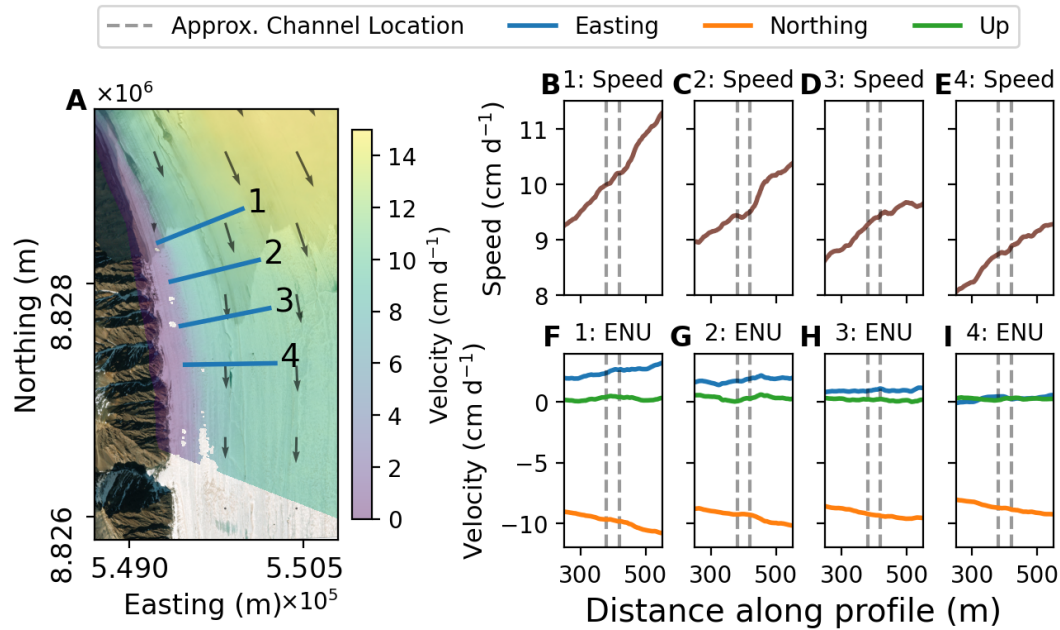
Fig. S5.   1-D profiles across the Upper Channel from 3-D inversion results from the 7 February 2018 and 3 March 2018 (ascending) and 31 January 2018 and 24 February 2018 (descending) scene pairs. (a) Location and number of each profile along with a velocity map. (b–e) The speed along each profile. (f–i) Profile velocity results, separated into ENU components. The dashed black lines in (b–i) indicate the approximate location of the channel as obtained from manual delineation of the channel in optical satellite imagery. Optical imagery courtesy of Esri World Imagery (Esri, 2022)

.

For the modeled heat flux F_t, we specify the heat flux (in $\mathrm{mWm^{-2}}$) as

$$f_1(x) = \begin{cases} 0 & y \leqslant 1200 \\[2mm] F_t & y > 1200, \end{cases} \tag{S1}$$

where y is the lateral position of the stream channel and F_t is prescribed (Table 1). The values of F_t are chosen in order to make the tributary ice up to $2°\mathrm{C}$ warmer or colder than it would otherwise be.

MODEL PARAMETER SELECTION

The points below detail the rationale behind selection of the model parameters.

Channel Depth (D_c): Maag (1963) mentions supraglacial streams in the Astro Lake vicinity that form channels of up to $30\,\mathrm{m}$ in depth. Thus, a range of channel depths up to $30\,\mathrm{m}$ are selected.

Surface Temperature (T_s): The range of surface temperatures is selected based on both the range of mean annual air temperature (MAAT) in the Canadian Arctic and a measurement of MAAT taken near the terminus of Thompson Glacier. Historical climate data indicate the MAAT for the Canadian Arctic Archipelago ranges from approximately $-10°\mathrm{C}$ to $-22°\mathrm{C}$ (McKenney and others, 2011). Temperature data recorded at Colour Lake ($176\,\mathrm{m}$ a.s.l.) in 1993, situated approximately 7 km SW of the Astro discontinuity ($\sim$300 m a.s.l.), showed a MAAT of $-15.2°\mathrm{C}$ (Doran and others, 1996). As the MAAT from Colour Lake is dated and recorded off-glacier, we select a fairly wide range of surface temperatures centered on the Colour Lake measurement but that capture the plausible temperature range for the Canadian Arctic as a whole.

Channel Temperature (T_c): The channel temperature approximates the yearly average temperature within the stream channel. The channel temperatures are selected based on three plausible scenarios. First, the channel temperature may match the surface ice temperature. Second, the flow of water in the stream for a significant portion of the year may cause the yearly average channel temperature to be warmer than the surface temperature. In addition, satellite imagery appears to show that the Astro Channel is covered by snow during winter, which potentially insulates the channel from the coldest winter air temperatures. To account for these two factors that would lead to channel temperatures above the MAAT, we test the cases where the channel is occupied by water

year round and thus at 0°C and where the channel is only seasonally occupied by water, perhaps with the insulating effects of snow cover, and thus between 0°C and the MAAT. Finally, cold air may pool in the channel leading to channel temperatures slightly lower than the surface ice temperature. For this scenario a value of 2 K lower than the surface ice temperature is selected. Several measurements of daytime air temperatures inside crevasses indicate that the temperature in the crevasse may be 4–5 K lower than the temperature of the glacier surface (Bhardwaj and others, 2016; Cook, 1956). As this temperature difference is likely at its maximum during the daytime due to shading provided by the crevasse walls, we select a slightly lower temperature depression for the cold air pooling scenario.

Tributary Heat Flux (F_t)**:** On Thompson Glacier, the ice east of the Astro Channel originates from Piper Glacier, a tributary that is both smaller and steeper than Thompson Glacier. Thus, it is plausible that the marginal (eastern) ice near the Astro Channel has a different temperature than the ice west of the stream. A temperature contrast is achieved by prescribing a small heat flux in the area east of the stream. These heat fluxes are chosen to correspond to maximum temperature difference of ± 2 K in 1 K increments.

Temperature Gradient Factor (G_t)**:** This coefficient is chosen to yield temperature profiles that are linear, concave up and concave down with a variety of gradients. Under steady state conditions, the temperature gradient in the ablation zone should be concave down. However, as Thompson Glacier is unlikely to be in steady-state, we test temperature gradients that are both concave down and concave up.

Sliding-Law Coefficient (C)**:** Basal motion, or lack thereof, will impact the magnitude of discontinuous motion. If the glacier is frozen to the bed everywhere, then no sliding will occur. Alternatively, some amount of sliding can occur along the central bed with only the glacier margin being frozen. In this case, a value of C (see (8)) is necessary to describe the basal friction. The values of C are selected to give a wide range of sliding ratios while resulting in sliding speeds that are physically realistic. Measuring values of C is prohibitively difficult as it requires knowing both the basal shear stress and basal sliding velocity, although estimates of C, often based on inversions of surface velocities, have been made (e.g, Minchew and others, 2016). The values of C used here are of the same order of magnitude as those presented in the literature (Minchew and others, 2016; Cuffey and Paterson, 2010).
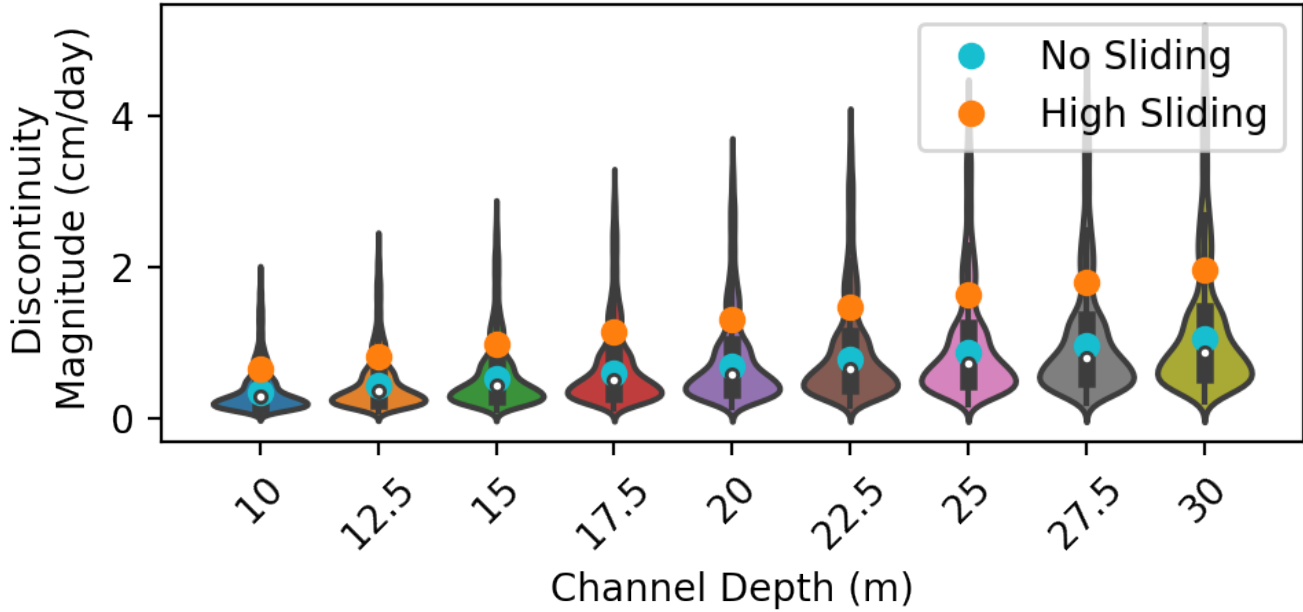
Fig. S6. Discontinuity magnitudes for modeled temperate glaciers with varying channel depths and sliding behaviors (orange and blue dots). For the high sliding case $C = 1.0 \times 10^8 \, \mathrm{Pa\,m\,s^{-1}}$. Also included are the distribution of discontinuity magnitudes for the modeled polythermal glaciers (violin plots).

100   **Thermal Transition Location (L_t):** One hypothesis to explain the Astro discontinuity is that

101   the horizontal position of the supraglacial channel roughly coincides with the location of a lateral

102   thermal transition at the bed and thus a basal slip-to-no-slip transition. Similar theories regarding

103   slip-to-no-slip transitions at glacier termini and their relation to thrust faulting, another form of

104   discontinuous glacier motion, have been investigated (Moore and others, 2010). In order to examine

105   the relationship between thermal transition location and discontinuity, we select a number of thermal

106   transition locations around $1200 \, \mathrm{m}$, the lateral position of the supraglacial channel. Note that the

107   thermal transition location L_t is defined as the distance from glacier center.

108 **ICE-FLOW MODELING RESULTS**

109 **Temperate glacier discontinuity magnitudes**

110 The ice-flow modeling results show that, on average, the temperate glaciers have larger discontinuity

111 magnitudes than their polythermal counterparts (See Fig. S6).
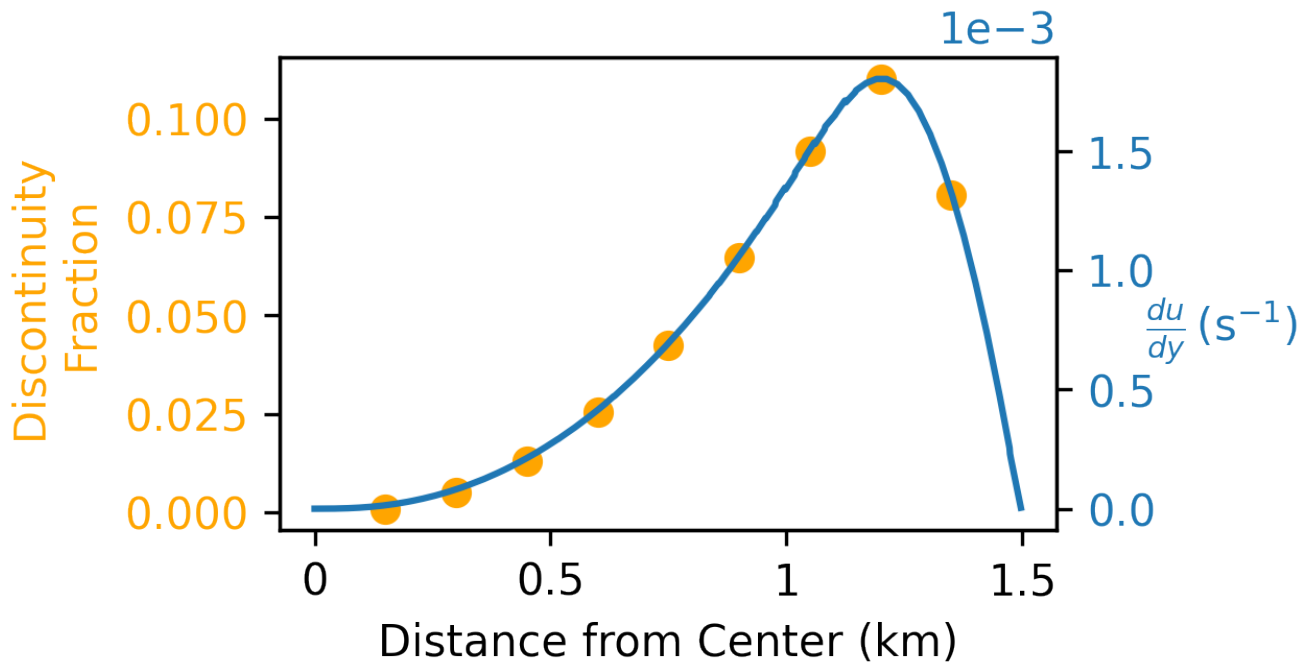
Fig. S7. The relationship between the discontinuity fraction for channels at various positions and the transverse velocity gradient. The thermal structure here is generated using $T_s = -15°\text{C}$, $T_c = -15°\text{C}$, $D_c = 20\,\text{m}$, $F_t = 0$, $G_t = 1/2$, $L_t = 1200\,\text{m}$ and C=None. The transverse velocity gradients are calculated by differencing consecutive velocity values, spaced $1\,\text{m}$ apart, from the west side of the glacier for a modeled glacier using the parameters above and a channel position that is $1350\,\text{m}$ east of center.

Velocity gradients and discontinuities

Intuitively, the transverse velocity gradient should be proportional to the discontinuity fraction for a glacier with a given thermal structure and sliding behavior. The end-member case in which the supraglacial channel is located at the glacier center can simply be solved using a symmetry argument. As the glacier is symmetrical about the center, both the velocity discontinuity and transverse velocity gradient must be zero. A simple test, in which the position of the supraglacial channel is varied for a glacier with a constant thermal structure, shows that the transverse velocity gradient and discontinuity magnitude are indeed proportional (Fig. S7)

REFERENCES

Bhardwaj A, Sam L, Singh S and Kumar R (2016) Automated detection and temporal monitoring of crevasses using remote sensing and their implications for glacier dynamics. *Annals of Glaciology*, **57**(71), 81–91. doi: 10.3189/

123   2016aog71a496

124 Cook JC (1956) Some observations in a Northwest Greenland crevasse. *Eos, Transactions American Geophysical*
125   *Union*, **37**(6), 715–718. doi: 10.1029/tr037i006p00715

126 Cuffey KM and Paterson WSB (2010) *The physics of glaciers.* Academic Press

127 Doran PT, McKay CP, Adams WP, English MC, Wharton RA and Meyer MA (1996) Climate forcing and thermal
128   feedback of residual lake-ice covers in the High Arctic. *Limnology and Oceanography*, **41**(5), 839–848. doi: 10.4319/
129   lo.1996.41.5.0839

130 Esri (2022) 'World Imagery' [basemap]. 15 m scale. Available at `www.arcgis.com/home/item.html?id=`
131   `10df2279f9684e4a9f6a7f08febac2a9` (September 23, 2022)

132 GLIMS Consortium (2005) Glims glacier database, version 1 doi: 10.7265/N5V98602

133 Maag HU (1963) Marginal drainage and glacier-dammed lakes

134 McKenney DW, Hutchinson MF, Papadopol P, Lawrence K, Pedlar J, Campbell K, Milewska E, Hopkinson RF,
135   Price D and Owen T (2011) Customized spatial climate models for North America. *Bulletin of the American*
136   *Meteorological Society*, **92**(12), 1611–1622. doi: 10.1175/2011bams3132.1

137 Minchew B, Simons M, Björnsson H, Pálsson F, Morlighem M, Seroussi H, Larour E and Hensley S (2016) Plastic
138   bed beneath Hofsjökull ice cap, central Iceland, and the sensitivity of ice flow to surface meltwater flux. *Journal*
139   *of Glaciology*, **62**(231), 147–158. doi: 10.1017/jog.2016.26

140 Moore PL, Iverson NR and Cohen D (2010) Conditions for thrust faulting in a glacier. *Journal of Geophysical*
141   *Research: Earth Surface*, **115**(F2). doi: 10.1029/2009jf001307

142 Porter C, Morin P, Howat I, Noh MJ, Bates B, Peterman K, Keesey S, Schlenk M, Gardiner J, Tomko K, Willis M,
143   Kelleher C, Cloutier M, Husby E, Foga S, Nakamura H, Platson M, Wethington J Michael, Williamson C, Bauer
144   G, Enos J, Arnold G, Kramer W, Becker P, Doshi A, D'Souza C, Cummens P, Laurier F and Bojesen M (2018)
145   ArcticDEM doi: 10.7910/DVN/OHHUKH